

Measurement of the neutron charge radius through the study of the nucleon excitation

A Jefferson Lab Proposal to PAC 49

H. Atac, A. Atencio, B. Duran, S. Jia, R. Li, M. Nycz, N. Sparveris (spokesperson)¹
Temple University, Philadelphia, PA 19122, USA

Z.E. Meziani
Argonne National Laboratory, Lemont, IL 60439, USA

A. Camsonne (spokesperson), D. Higinbotham, M. Jones (spokesperson)
Thomas Jefferson National Accelerator Facility, Newport News, VA, USA

M. Paolone (spokesperson)
New Mexico State University, Las Cruces, NM, USA

M. Katramatou, G. Petratos
Kent State University, Kent, OH 44240, USA

W. Lin, R. Gilman, O. Yeung
Rutgers University, Piscataway, NJ 08855, USA

A. Christopher, T. Gautam, M. Kohl, J. Nazeer, T. Patel, M. Rathnayake, M Suresh
Hampton University, Hampton, Virginia 23668, USA

M. Mihovilovič, S. Širca
University of Ljubljana, Slovenia Jožef Stefan Institute, 1000 Ljubljana, Slovenia

¹contact:sparveri@temple.edu

Abstract

The neutron is a cornerstone in our depiction of the visible universe. The precise measurement of its charge radius, one of systems most fundamental properties, is an essential part of unraveling the neutron structure. Despite the neutrons net zero electric charge, the asymmetric distribution of the positively-charged (up) and negatively-charged (down) quarks in the system lead to a negative $\langle r_n^2 \rangle$. Thus, the precise determination of the charge radius offers insight to the contribution from the u- and d-quarks and provides valuable access to the nucleon dynamics. The determination of $\langle r_n^2 \rangle$ has relied in the past on measurements of the neutron-electron scattering length, b_{ne} , from neutron scattering off electrons bound in diamagnetic atoms. Nevertheless, the world data exhibit discrepancies that point to a potential underestimation of the method's systematic uncertainties. With this proposal, that follows the LOI-12-20-002, we aim to perform an electron scattering measurement of the neutron mean square charge radius, $\langle r_n^2 \rangle$. The proposed experiment will employ a recently proposed method¹. It will utilize the SHMS and the HMS spectrometers in Hall C and will allow to access with high precision the $N \rightarrow \Delta$ transition form factors, the neutron electric form factor G_E^n at very low momentum transfers, and to extract the $\langle r_n^2 \rangle$ through the slope of G_E^n at $Q^2 \rightarrow 0$. The proposed measurements will access $\langle r_n^2 \rangle$ at the $\sim 3.7\%$ level, and will offer new input toward addressing the long standing discrepancies in r_n measurements. The measurements will test the electron-scattering based charge-radius extraction on the isospin partner of the proton, whose corresponding charge radius measurements have been questioned recently in light of the proton radius puzzle. The new G_E^n data will allow the flavor decomposition of the nucleon electromagnetic form factors at low momentum transfers, and from the derivative of the flavor dependent Dirac form factors at $Q^2 = 0$ the mean square radii of the quark distributions in the nucleon will be directly determined. Furthermore, the measurement of the $N \rightarrow \Delta$ transition form factors at the low momentum transfer region will study the nucleon dynamics and the mechanisms responsible for the presence of non-spherical components in the nucleon wavefunction, in a region where the mesonic cloud dynamics is predicted to be dominant and rapidly changing, and will offer a test bed for chiral effective field theory calculations.

1 Introduction

The neutron represents a cornerstone in the understanding of nature. It naturally holds a central role in the understanding of hadronic matter, being one of the two facets of the nucleon, which in-turn accounts for $\sim 99\%$ of the visible matter in the Universe. More than that, the neutron holds a central role at larger scales, since its properties are decisive in the formation of the cosmological theories. The nucleon charge radius is one of its most important properties, and its study has been historically instrumental towards the understanding of the nucleon structure. For the neutron, despite its net zero electric charge, the asymmetric distribution of the positively-charged (up) and negatively-charged (down) quarks in the system lead to a negative $\langle r_n^2 \rangle$. Thus, the precise determination of the charge radius offers insight to the contribution from the u- and d-quarks and provides valuable access to the nucleon dynamics. Employing different techniques in extracting this fundamental quantity has proven most valuable, as recently exhibited in the case of the proton. The recent disagreement of the proton charge radius, r_p , as determined using the measurement of the Lamb shift in the muonic hydrogen atom², with the earlier results based on the hydrogen atom and the electron scattering measurement, gave rise to the proton radius puzzle³. This, in turn, led to a significant reassessment of the methods and analyses utilized in the radius extraction, and to the consideration of physics beyond the standard model as potential solutions to resolve this discrepancy. For the neutron, the isospin partner of the proton, the r_n determination is more challenging. Here one can not employ the multiple techniques that have been applied for the proton radius extraction, since no equivalent atomic method is possible and the electron scattering method suffers from severe limitations due to the absence of a free neutron target. The extraction of r_n has been uniquely based on a rather indirect method, the measurement of the neutron-electron scattering length b_{ne} , where low-energy neutrons are scattered by electrons bound in diamagnetic atoms. The world data exhibit discrepancies and the b_{ne} measurements in the world literature have been compiled in two different groups^{4–6}, the $b_{ne} = -(1.31 \pm 0.03) 10^{-3}$ (fm) (Garching-Argonne) and the $b_{ne} = -(1.59 \pm 0.04) 10^{-3}$ (fm) (Dubna), based on their systematic differences. This 5σ discrepancy is in-turn directly translated into an equivalent discrepancy of the extracted $\langle r_n^2 \rangle$, as shown in Fig. 1. The $\langle r_n^2 \rangle$ measurements adopted by PDG^{4,7–9}, the most recent of which is dated two decades ago, consider only a fraction of the world data and also exhibit discrepancies, with the values ranging from $\langle r_n^2 \rangle = -0.115 \pm 0.002 \pm 0.003$ (fm^2)⁴ to $\langle r_n^2 \rangle = -0.134 \pm 0.009$ (fm^2)⁸. The PDG world data average value thus becomes somewhat elusive, since it averages measurements that disagree. The underestimated systematic uncertainties associated with this method of extraction have been widely acknowledged and they have puzzled the physics community for two decades. Among the plausible explanations that have been suggested for this one can find the effect of resonance corrections and of the electric polarizability, as discussed e.g. in⁷, but these discrepancies have not been fully resolved. More recently, the neutron-electron scattering length results have been discussed for their potential to offer constraints to hypothetical new short-range interactions⁶ but the observed discrepancies of the b_{ne} data do not allow at the moment any such reliable constraints⁶. In that context, it has been suggested that measuring the neutron charge radius through the neutron electric form factor could offer the solution to this problem⁶.

The alternative path to determine the neutron charge radius is offered by measuring the slope of the neutron electric form factor, G_E^n , at $Q^2 \rightarrow 0$, which is proportional to $\langle r_n^2 \rangle$. In the past, determinations of G_E^n at finite Q^2 were typically carried out by measuring double polarization observables in quasi-elastic electron scattering from polarized deuterium or 3He targets using polarized electron beams^{10–23}. However, these measurements were not able to access G_E^n at a sufficiently low Q^2 range for the slope, and subsequently the $\langle r_n^2 \rangle$, to be determined. Here we propose to employ a recently proposed method¹ to access G_E^n , that takes advantage of the fundamental symmetry of the neutron and the proton, as opposed to relying

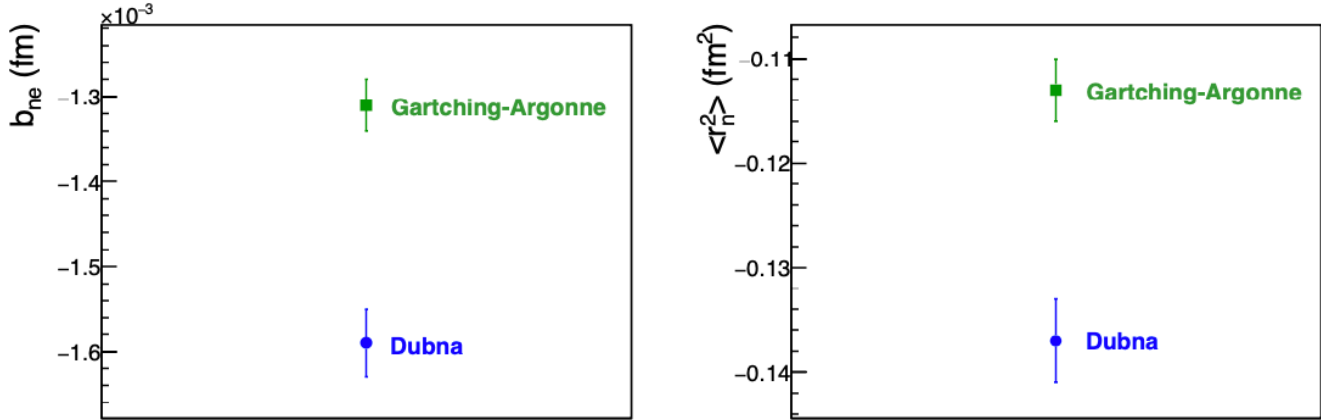


Figure 1. The two b_{ne} compilations^{4–6} of the world data (left) and the corresponding $\langle r_n^2 \rangle$ extractions based on these measurements (right).

on measurements with few-body nuclear targets that was done in the past. It has long been known^{24,25} that the ratios of the quadrupole to the magnetic dipole transition form factors of the proton, $C2/M1$ and $E2/M1$, are fundamentally related to the neutron elastic form factors ratio G_E^n/G_M^n . The transition form factors can be measured with high precision at low momentum transfers, as recent experiments have shown^{26–30}. This, in-turn, opens up the path to access the G_E^n at low momentum transfers and to determine the $\langle r_n^2 \rangle$ from the G_E^n slope at $Q^2 = 0$.

2 General considerations

Since the submission of the LOI-12-20-002, the collaboration has worked on a detailed study of experimental, theoretical, and technical parameters, so that their effect and impact on the proposed measurements can be quantified. For clarity, we briefly summarize these studies here:

- A complete study of the proposed method has been performed and published at¹. The theoretical uncertainties associated with the extraction of the G_E^n have been quantified and they are smaller compared to the corresponding experimental uncertainties.
- The extraction of the neutron charge radius from the fits of the G_E^n slope at $Q^2 \rightarrow 0$ allows the determination of the $\langle r_n^2 \rangle$ within $\sim 3.7\%$ when all (experimental and theoretical) uncertainties in the observables have been considered in the fits. Detailed studies have also been performed for the suitability and for the fitting ranges of the fitted functional forms.
- We have analyzed recent data of the same reaction channel that is proposed here, utilizing the same experimental setup (namely with SHMS and HMS measuring electrons and protons in coincidence, respectively). The data were taken parasitically during the running of the E12-15-001 (VCS) experiment, at a slightly higher momentum transfer of $Q^2 = 0.3$ (GeV/c)², where the cross section is well known. The cross section results have demonstrated our excellent understanding of the coincidence acceptance within the simulation, the good handle of the systematic uncertainties, as well as the readiness of all the experimental and theoretical tools involved in this effort.
- The effect of the lower than typical proton momenta at the HMS has been studied. Resolution effects have been explored with simulation studies and the influence on the measured cross sections, from

all the systematic effects, has been quantified. The overall systematic uncertainty on the measured cross sections is expected to be better than 4%.

3 $N \rightarrow \Delta$ transition form factors

The first excited state of the nucleon dominates many nuclear phenomena at energies above the pion-production threshold and plays a prominent role in the physics of the strong interaction. The study of the transition form factors in-turn has allowed to explore various aspects of the nucleonic structure. Hadrons are composite systems with complex quark-gluon and meson cloud dynamics that give rise to non-spherical components in their wavefunction, which in a classical limit and at large wavelengths will correspond to a “deformation”^{31–33}. The determination and subsequent understanding of the shapes of the fundamental building blocks in nature is a particularly fertile line of investigation for the understanding of the interactions of their constituents amongst themselves and the surrounding medium. For hadrons this means the interquark interaction and the quark-gluon dynamics. For the proton, the only stable hadron, the vanishing of the spectroscopic quadrupole moment, due to its spin 1/2 nature, precludes access to the most direct observable of deformation. As a result, the presence of the resonant quadrupole amplitudes $E_{1+}^{3/2}$ and $S_{1+}^{3/2}$ (or E2 and C2 photon absorption multipoles respectively) in the predominantly magnetic dipole $M_{1+}^{3/2}$ (or M1) $\gamma^* N \rightarrow \Delta$ transition has emerged as the experimental signature for such an effect^{26–67}. Nonvanishing quadrupole amplitudes will signify that either the proton or the $\Delta^+(1232)$ or more likely both are characterized by non-spherical components in their wavefunctions. These amplitudes have been explored up to four momentum transfer squared $Q^2 = 7$ (GeV/c)²^{26–30,37–45,45–50,56–60} and the experimental results are in reasonable agreement with models invoking the presence of non-spherical components in the nucleon wavefunction.

In the constituent-quark picture of hadrons, the non-spherical amplitudes are a consequence of the non-central, color-hyperfine interaction among quarks^{32,35}. However, it has been shown that this mechanism only provides a small fraction of the observed quadrupole signal at low momentum transfers, with the magnitudes of this effect for the predicted E2 and C2 amplitudes³⁶ being at least an order of magnitude too small to explain the experimental results and with the dominant M1 matrix element being $\approx 30\%$ low. A likely cause of these dynamical shortcomings is that such quark models do not respect chiral symmetry, whose spontaneous breaking leads to strong emission of virtual pions (Nambu-Goldstone Bosons)³⁴. These couple to nucleons as $\vec{\sigma} \cdot \vec{p}$ where $\vec{\sigma}$ is the nucleon spin, and \vec{p} is the pion momentum. The coupling is strong in the p wave and mixes in non-zero angular momentum components. Based on this, it is physically reasonable to expect that the pionic contributions increase the M1 and dominate the E2 and C2 transition matrix elements in the low Q^2 (large distance) domain. This was first indicated by adding pionic effects to quark models^{61–63}, subsequently in pion cloud model calculations^{52,53}, and recently demonstrated in Chiral Effective Field Theory calculations⁶⁴. With the existence of these non-spherical amplitudes well established, recent high precision experiments and theoretical efforts have focused on testing in depth the reaction calculations and decoding the underlying nucleon dynamics. The proposed measurements focus on the low momentum transfer region, where the mesonic cloud dynamics is predicted to be dominant and rapidly changing (e.g. see Fig. 2), offering a test bed for chiral effective field theory calculations. Furthermore, the new measurements will allow to test the theoretical prediction that the Electric and the Coulomb quadrupole amplitudes converge as $Q^2 \rightarrow 0$.

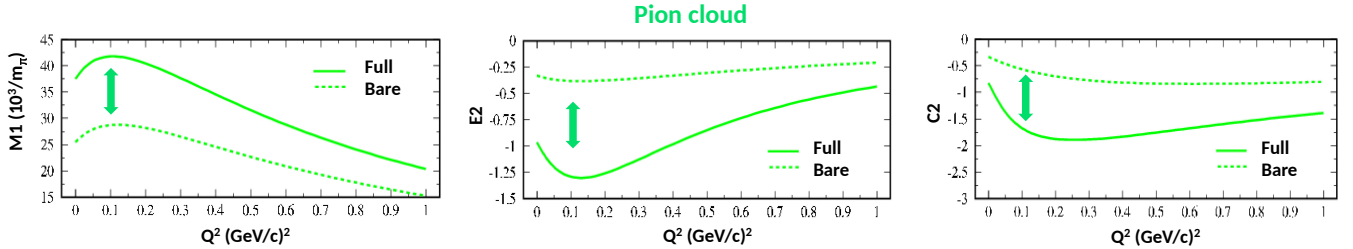


Figure 2. The effect of the pion cloud to the resonant amplitudes as predicted by the Sato Lee calculation (Bare: without the pion cloud).

4 Extraction of G_E^n

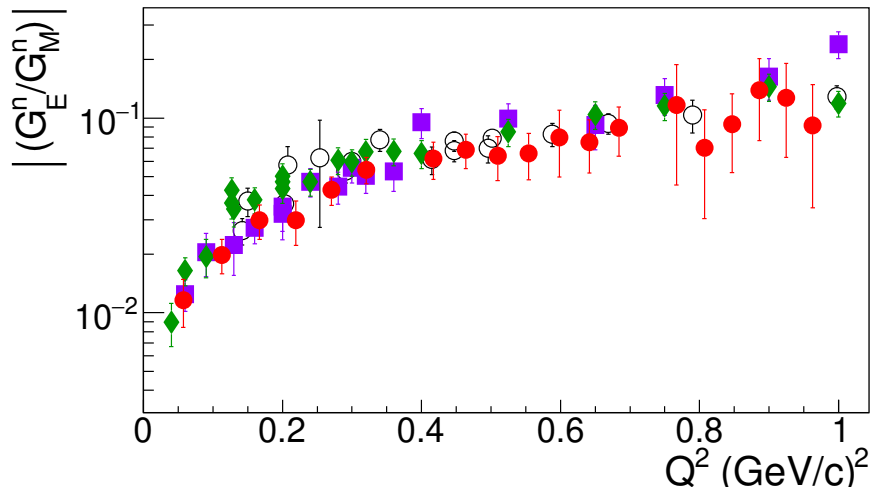
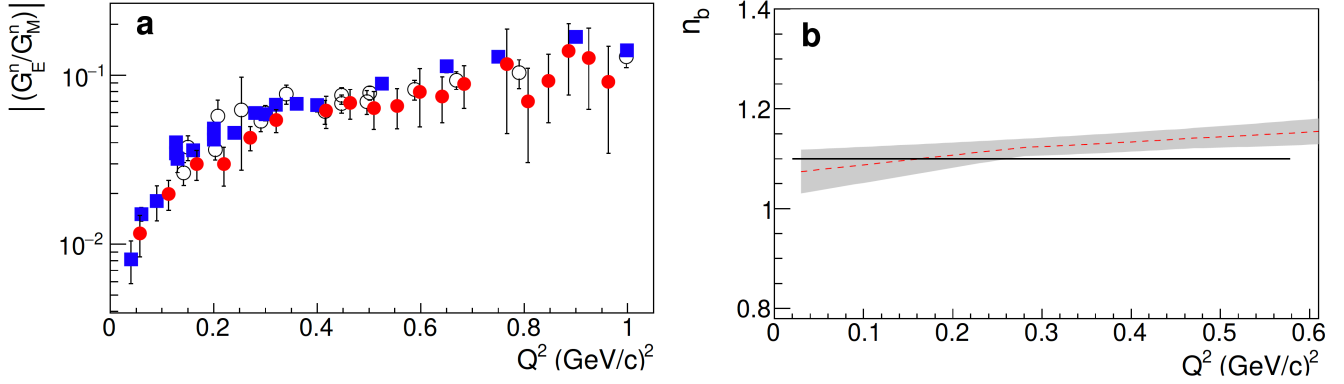
The neutron elastic form factors ratio G_E^n/G_M^n has long been known^{24,25} to be fundamentally related to the ratios of the quadrupole to the magnetic dipole transition form factors of the proton. The connection has been established through multiple relationships and allows the G_E^n/G_M^n determination from the transition form factor measurements with a theoretical uncertainty at the 10%-15% level. The potential of this avenue towards the study of the neutron charge radius has been presented in¹. Below, the theoretical framework is briefly summarized and its validity is observed through the analysis of the form factor world data.

A consequence of the SU(6) spin and flavor symmetry group in which the nucleon and the Δ resonance belong leads to the following expression²⁴

$$\frac{G_E^n(Q^2)}{G_M^n(Q^2)} = \frac{Q}{|q|} \frac{2Q}{M_N} \frac{1}{n_b(Q^2)} \frac{C2}{M1}(Q^2) \quad (1)$$

where q is the virtual photon three-momentum transfer magnitude in the γN center of mass frame, M_N is the nucleon mass. The n_b term accounts for three-quark current terms that tend to slightly increase the $C2/M1$ ratio (or correspondingly decrease the G_E^n/G_M^n), an SU(6) symmetry breaking correction that has been theoretically quantified to $\approx 10\%$ ²⁴ (i.e. $n_b \approx 1.1$). Here, one can adopt the most conservative path, where a theoretical uncertainty can be assigned to this term that is equal to the full magnitude of the theoretically predicted symmetry breaking contributions, namely $n_b = 1.1 \pm 0.1$. Considering the confidence with which the underlying theory is able to determine the level of the symmetry breaking contributions, the above assumption leads to a safe estimation (and possibly to an overestimation) of the theoretical uncertainty.

The wealth of experimental data acquired in recent years, namely for G_E^n/G_M^n ^{10–23} and for the $C2/M1$ ^{26–30,47,49,56,58} allow stringent tests to the validity of this fundamental connection. Using the world data one can test the validity of Eq. 1, as well as to experimentally determine the magnitude of the n_b contribution, within the kinematic range where both the elastic and the transition form factors have been extensively measured. In Fig. 3a the G_E^n/G_M^n world data^{10–23} are shown. In order to explore the validity of this relationship we utilize Eq. 1 so as to derive the G_E^n/G_M^n ratios from the $C2/M1$ measurements^{26–30,47,49,56,58} and we compare the results to the neutron G_E^n/G_M^n world data; here we assume that $n_b = 1$, i.e. no correction is employed for that part of the symmetry breaking contributions. The $n_b(Q^2)$ can then be determined experimentally, by parametrizing the two data sets, $F_R(Q^2)$ and $F_R^*(Q^2)$ respectively, and forming their ratio $n_b(Q^2) \equiv F_R^*(Q^2)/F_R(Q^2)$. A variety of functional forms has been employed so as to identify those that can provide a good fit to the data and all the appropriate functions are then considered in the determination of n_b . To that end, one can identify the following groups of



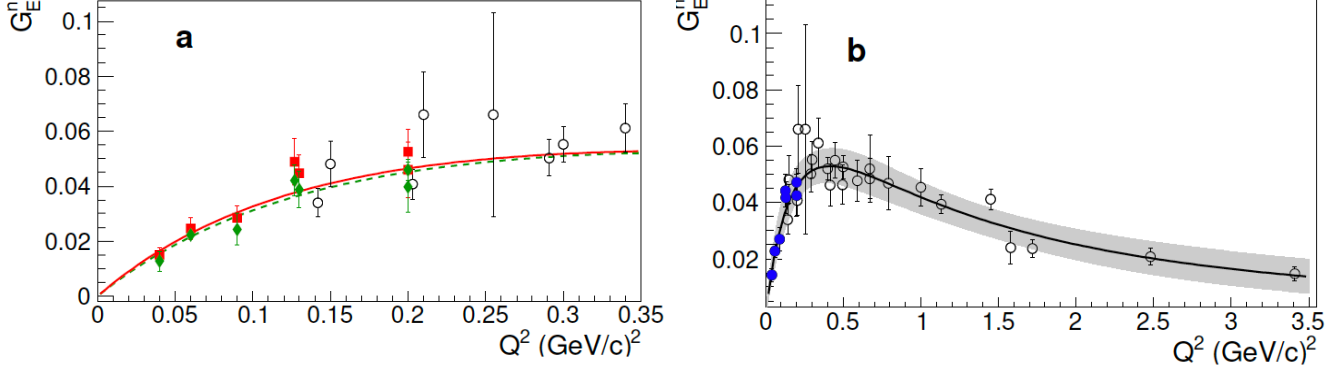


Figure 5. a) Green diamonds: the G_E^n results from the SU(6)²⁴ analysis of the measurements^{26–30}. Red boxes: the G_E^n results from the Large- N_c ²⁵ analysis of the data. The fit to the data from the parametrization of Eq. 6 is shown with the dashed and the solid curves, respectively.
b) Blue circles: The final G_E^n results extracted from the weighted average result of the SU(6) and the large- N_c analysis of the^{26–30} measurements. The variance of the two data sets is quantified as a theoretical uncertainty. The solid curve shows the fit to the data from the parametrization of Eq. 6, with its uncertainty (shaded band). The G_E^n world data (open-circles)^{10–23} are also shown.

functional forms that are able to provide a good fit to the data:

$$F_R(x) = \sum_{i=1}^j a_i x_i^i, \quad F_R(x) = \frac{\sum_{i=1}^j b_i x_i^i}{(1 + \sum_{j=1}^k c_j x_j^j)}, \quad F_R(x) = (1 - \exp^{(d_1 x)}).$$

Once all of the functional forms have been considered, one can derive $n_b(Q^2)$ from the experimental data, as shown in Fig. 3b; here the n_b -variance due to the choice of parametrization is quantified as an uncertainty and is illustrated as an uncertainty band. In order to further refine this procedure, at low momentum transfers where neutron data do not exist, we have extracted the ratio G_E^n/G_M^n from numerical simulations within lattice Quantum Chromodynamics (LQCD) using the G_E^n and G_M^n data of Ref⁶⁸. The LQCD data provide input on the Q^2 -dependence of the G_E^n/G_M^n ratio based on ab-initio QCD calculations and they allow for further guidance to the parametrization of the neutron data. This step ultimately leads to a rather small refinement of ≤ 0.003 in the determination of $n_b(Q^2)$.

The LQCD results exhibit a remarkable agreement with the experimental world data, as shown in Fig. 3a. The parameters of the LQCD calculation are such that they reproduce the physical value of the pion mass. Thus, such a calculation eliminates a major source of systematic uncertainties, that is, the need of a chiral extrapolation. Furthermore the lattice results include both the connected and disconnected diagram, and therefore G_E^n and G_M^n include both valence and sea quark contributions.

The experimentally determined $n_b(Q^2)$ is in excellent agreement with the theoretical prediction²⁴, as seen in Fig. 3b, and offers strong credence to the underlying theory²⁴. As indicated by the width of the uncertainty band in Fig. 3b, the $n_b(Q^2)$ uncertainty compares a factor of two smaller to the most conservative assumption of $n_b = 1.1 \pm 0.1$. For the analysis of the proposed projected measurements, we have consider the G_E^n extraction under both scenarios i.e. one with $n_b = 1.1 \pm 0.1$, and one with the n_b as determined from the experimental world data (Fig. 3b). The two sets of results come to a remarkable agreement ($\leq 3\%$) that is much smaller compared to the overall G_E^n uncertainty. A mildly improved G_E^n uncertainty is obtained in the latter case, due to a smaller level of the n_b uncertainty. This in-turn leads

to a slightly improved r_n -uncertainty; nevertheless this difference is not a leading factor and has a small consequence in the final r_n extraction.

The uncertainty of the extracted G_E^n is driven by the following factors:

1. Experimental (statistical and systematic) uncertainties in the determination of $C2/M1$.
2. Model uncertainty in the determination of $C2/M1$. This is due to the presence of non-resonant pion electro-production amplitudes that interfere with the extraction of the resonant amplitudes. These effects have been studied by employing theoretical pion electro-production models^{52–54, 69, 70} in the data analysis (e.g. see Refs.^{26–30}). The level of control over this uncertainty has been experimentally tested, by measuring $C2/M1$ through an alternative reaction channel, the $p(e, e' p)\gamma^0$, were one employs a different theoretical framework for the ratio extraction.
3. The uncertainty of the symmetry breaking contributions δn_b , as discussed earlier in this section.
4. In order to extract the G_E^n from the G_E^n/G_M^n ratio, we have to use a parametrization of the well known G_M^n , as typically done in such cases (e.g.^{12, 19} etc). Here we have used the one from Ref.⁷¹. We have studied the associated uncertainty by employing different G_M^n -parametrizations in our analysis and we have found that it accounts for a small fraction of the total uncertainty.

The alternative path that leads to the relation between the G_E^n and the quadrupole transition form factors has been established through large- N_c relations²⁵. These relations take the form

$$\frac{E2}{M1}(Q^2) = \left(\frac{M_N}{M_\Delta}\right)^{3/2} \frac{M_\Delta^2 - M_N^2}{2Q^2} \frac{G_E^n(Q^2)}{F_2^p(Q^2) - F_2^n(Q^2)} \quad (2)$$

$$\frac{C2}{M1}(Q^2) = \left(\frac{M_N}{M_\Delta}\right)^{3/2} \frac{Q_+ Q_-}{2Q^2} \frac{G_E^n(Q^2)}{F_2^p(Q^2) - F_2^n(Q^2)} \quad (3)$$

where $F_2^{p(n)}$ are nucleon's Pauli form factors, M_Δ is the mass of the Δ , and $Q_\pm = ((M_\Delta \pm M_N)^2 + Q^2)^{\frac{1}{2}}$. Here one is free from any additional correction terms, such as the symmetry breaking contributions of Eq. 1. A second advantage is that the experimental data base is extended to include the Electric quadrupole (E2) transition, which in turn allows for an improved extraction of the G_E^n . Being able to extract the G_E^n independently through the Coulomb and the Electric quadrupole transitions offers a strong experimental test to the validity of the theoretical relations and allows to validate their level of theoretical uncertainty. The above relations come with a 15% theoretical uncertainty²⁵ that is treated accordingly in the G_E^n analysis. The G_E^n extraction from the Coulomb and from the Electric quadrupole transitions world data agree nicely within that level, as can be seen in Fig. 4, thus confirming the validity of the theoretical framework. For the well known G_E^p , G_M^p and G_M^n that enter in the expressions through the Pauli form factors we use recent parametrizations; for the G_M^p and G_M^n we use⁷¹, while for G_E^p we performed an updated parametrization so that we may include recent measurements from⁷² that were not yet available in⁷¹ using the widely used functional form

$$G_E^p = \frac{1 + \left(\sum_{i=1}^2 a_i x_i^i \right)}{\left(1 + \sum_{j=1}^4 b_j x_j^j \right)}. \quad (4)$$

The potential of the proposed method for the G_E^n extraction has been exhibited through an analysis¹ that utilizes the JLab/Hall-A and MAMI/A1 measurements^{26–30} that extend as low as $Q^2 = 0.04 \text{ (GeV}/c)^2$, in a kinematical region similar and partially overlapping to the proposed measurements. The results of the SU(6) based analysis and of the large- N_c analysis is in remarkable agreement as exhibited in Fig. 5(a), by the red and green points, respectively. The weighted average of the two values leads to the final G_E^n result that is shown in Fig. 5(b) (blue circles). Here, the variance of the results from the two different analyses is assigned as an additional, theoretical, uncertainty for G_E^n .

5 Neutron charge radius extraction

The neutron mean square charge radius is related to the slope of the neutron electric form factor as $Q^2 \rightarrow 0$ through

$$\langle r_n^2 \rangle = -6 \frac{dG_E^n(Q^2)}{dQ^2} \Big|_{Q^2 \rightarrow 0}. \quad (5)$$

The $G_E^n(Q^2)$ has to be parametrized and fitted to the experimental data, and from the slope at $Q^2 = 0$ the $\langle r_n^2 \rangle$ is determined. Our studies, utilizing the projected measurements from this proposal and the low- Q^2 G_E^n data¹ from the analysis of the JLab/Hall-A and MAMI/A1 measurements^{26–30}, have shown that the most robust function for the radius extraction takes the form

$$G_E^n(Q^2) = (1 + Q^2/A)^{-2} \frac{B\tau}{1 + C\tau}, \quad (6)$$

where $\tau = Q^2/4m_N^2$, and A, B, C are free parameters. It has a similar form to the long standing phenomenological Galster parametrization⁷³, where instead of using the standard dipole form factor with $\Lambda^2 = 0.71 \text{ (GeV}/c)^2$ an additional free parameter A is introduced (see Eq. 6). A second parametrization, giving a good fit to the data, involves the sum of two dipoles

$$G_E^n(Q^2) = \frac{A}{(1 + \frac{Q^2}{B})^2} - \frac{A}{(1 + \frac{Q^2}{C})^2}. \quad (7)$$

This form has been exploited in the past¹⁹ but with the $\langle r_n^2 \rangle$ already constrained by the measurement of the neutron-electron scattering length b_{ne} . Here we have removed the constraint on the neutron charge radius and we consider three parameter fits that rely only on electric form factor data. The fitted results of the two parametrizations come to an excellent agreement; the two curves are nearly indistinguishable by eye, resulting to a nearly identical result for the r_n . The validity of both functions has been further explored with studies which involve fits with pseudo-data sets. These studies have revealed that the two-dipole fit suffers from certain limitations in the determination of the radius that are not present in the fits with Eq. 6. For that reason, we will adopt only the paramterization of Eq. 6 for the extraction of $\langle r_n^2 \rangle$.

The $\langle r_n^2 \rangle$ extraction can also be explored through fits within a limited range at low- Q^2 where G_E^n evolves monotonically (i.e. lower than $Q^2 = 0.4 \text{ (GeV}/c)^2$), rather than with fits over the full Q^2 -range of the world data. In this case, fits with multiple functional forms¹ and within a varying fitting range have to be considered for the $\langle r_n^2 \rangle$ extraction. Our studies have shown that the low- Q^2 fits can provide the $\langle r_n^2 \rangle$ at the same level of precision as the fits over the full Q^2 -range, thus offering an additional control over the model dependence of the fitted result.

Lastly, the radius extraction has been explored by employing multiple G_M^n parametrizations, so that the uncertainty associated with the choice of the G_M^n parametrization can be quantified. Our studies have shown that this uncertainty is approximately an order of magnitude smaller compared to the total $\langle r_n^2 \rangle$ uncertainty.

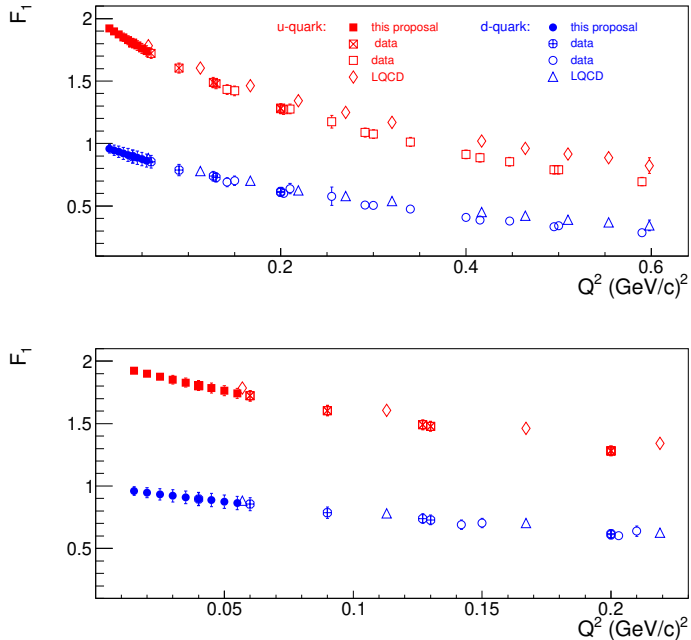


Figure 6. The projected measurements from the u- and d-quark flavor decomposition of the F_1 form factor. The F_1 form factor as derived for the neutron world data from the polarization measurements (empty-symbols) and from the G_E^n data of the¹ (empty-crossed-symbols) is shown. The LQCD results that have been extracted using the data of⁶⁸ are also shown on the figure.

6 Flavor dependent form factors

The proposed G_E^n measurements will allow a unique insight into the flavor decomposition of the elastic nucleon electromagnetic form factors at low Q^2 and to the mean square radii of the quark distributions in the nucleon. To that end, one can follow the same line of work as previously done in- Q^2 ^{74,75}. Starting from the Dirac and Pauli nucleon form factors $F_1^{p(n)}$ and $F_2^{p(n)}$, under charge symmetry we perform the flavor decomposition of the form factors using the relations

$$F_{1(2)}^u = 2F_{1(2)}^p + F_{1(2)}^n \quad F_{1(2)}^d = 2F_{1(2)}^n + F_{1(2)}^p \quad (8)$$

where with $F_{1(2)}^u$ and $F_{1(2)}^d$ we refer to the up and down quark contributions to the Dirac (Pauli) form factors of the proton. The normalizations of the Dirac form factors at $Q^2 = 0$ are given by $F_1^u(0) = 2$ and $F_1^d(0) = 1$ so as to yield a normalization of 2 and 1 for the u and the d -quark distributions in the proton, respectively. For the Pauli form factors at $Q^2 = 0$ the normalizations are given by $F_2^q(0) = \kappa_q$, where κ_u and κ_d can be expressed in terms of the proton (κ_p) and neutron (κ_n) anomalous magnetic moments as $\kappa_u \equiv 2\kappa_p + \kappa_n = +1.67$ and $\kappa_d \equiv \kappa_p + 2\kappa_n = -2.03$. The proposed measurements will extend the flavor decomposition of the form factors at low Q^2 , as seen in Fig. 6. Each data point corresponds to a G_E^n measurement, while for G_E^p , G_M^p and G_M^n a parametrization is utilized, as described earlier. The slopes of the flavor dependent Dirac form factors at $Q^2 = 0$ are related to the mean square radius of the quark distributions

$$\langle b_{u(d)}^2 \rangle = \frac{-4}{F_1^{u(d)}(0)} \left. \frac{dF_1^{u(d)}(Q^2)}{dQ^2} \right|_{Q^2 \rightarrow 0} \quad (9)$$

where b denotes the quark position in the plane transverse to the longitudinal momentum of a fast moving nucleon. The mean square radii of the quark distributions are naturally related to the proton and to the neutron charge radii in a model independent way, and one can derive them, indirectly, from the measured values of the nucleon's charge radii. Here we can directly extract these quantities with high precision, by fitting the experimental $F_1^{u(d)}$ data.

7 The Experiment

7.1 Experimental apparatus and set-up

The experiment will involve measurements of the $p(e, e' p)\pi^0$ reaction. In an experimental arrangement as shown in Fig. 7, the SHMS and the HMS will detect electrons and protons, respectively. The undetected pion will be identified through the missing mass reconstruction. The spectrometers will employ their standard detector packages which are shown in Fig. 8 and Fig. 9 for the HMS and SHMS. For the SHMS, the Argon/Neon Cerenkov would be replaced by a vacuum pipe which is an additional standard SHMS detector stack configuration. This will reduce the multiple scattering before the SHMS drift chambers and improve the missing mass resolution. The target requested is a 4 cm LH2 cell, while the beam current will be ranging from 6 μA to 15 μA . With the small expected π^- to electron rate (see Table 2) the calorimeter alone in the SHMS will provide all the needed π^- from electron separation. With the proton's momenta under 1.0 GeV/c, timing information will be more than sufficient to separate protons from π^+ 's in the HMS. Dedicated optics runs will be required for the SHMS spectrometer since it will acquire data in momenta around 1 GeV/c, as well as a set of elastic runs for calibration and normalization purposes. The beam energy required is 1.3 GeV for all kinematic settings.

We have investigated the issues raised in the technical response to the LOI. The first point in the technical response raised issue with the ramifications of low momentum protons in the HMS. For the kinematics of the experiment, the coincidence time difference between the two spectrometers will vary from 90 to 170ns as the proton momentum varies from 380 to 570 MeV/c. The experiment will have to change the timing between the two arms at the trigger for each kinematic setting to center the HMS trigger within the SHMS trigger window. We plan to run with the SHMS trigger window with width of 60ns and the HMS trigger window width a width of 20ns. At HMS central momentum of 388 MeV/c, the protons at the large negative delta region will stop in the last scintillator plane. We agree that the protons are far way from minimum ionizing region and the pulse heights in the scintillators will be larger than usually seen in Hall C experiments. We plan on running the HMS scintillators at low high voltages and determining the optimal HV for running at this low momentum. We plan to take elastic coincidence data between the electron and proton with SHMS at the momentum ranges of the experiment to determine the trigger efficiency.

The second point in the technical response is about the stability of the HMS quadrupoles at the low momentum. We have discussed this with Steve Lassiter. Danfysik has stated that the power supplies will regulate at 2% of the maximum which is about 25A. For 388 MeV/c central momentum, HMS Q3 is at the lowest current of 19A with Q1 and Q2 at 40 and 50A. Since Q3 is near the 2% limit, we have asked Steve Lassiter to do stability test of all the quads with their new power supplies during the summer 2021. Investigations into the effects of the magnetic hysteresis at this low fields will be studied at the same time. One remark here is that the HMS was operated to momentum of 440 MeV/c during the summer of 2019 for an experiment. The sieve slit data showed the expected resolution effects from multiple scattering and the focal plane distribution did not show a change when the momentum changed from 1 GeV/c to 0.44 GeV/c. This indicates the optics of the HMS scale properly. If need be, we can adjust the lowest momentum setting from 388 MeV/c to a similar momentum range above 400 MeV/c. We have performed

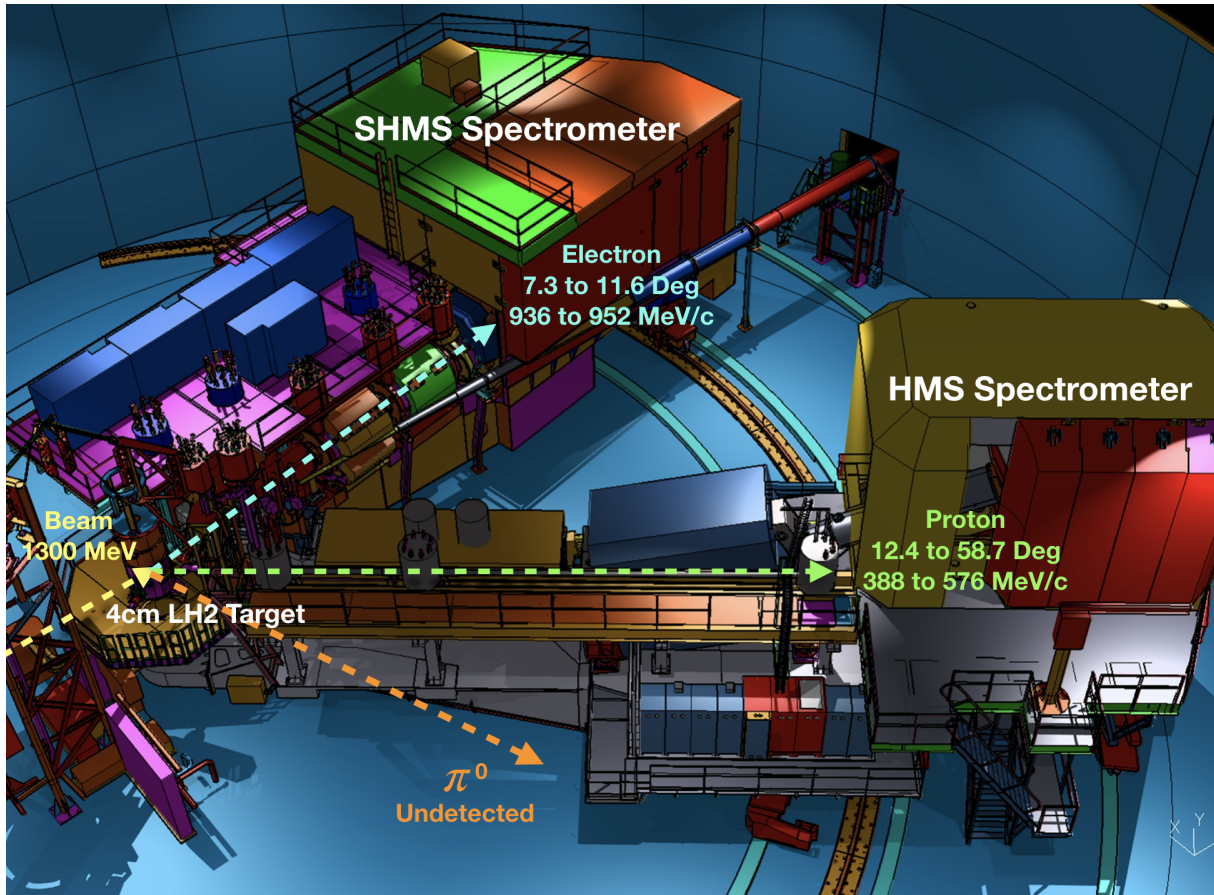


Figure 7. An illustration of the experimental hall and the proposed kinematic settings in Hall-C. See Tab. 1 for exact central angle and central momentum settings for each spectrometer arm.

studies to identify what will be the effect on the results in such a case, and we have identified a $< 10\%$ impact to the uncertainty of the extracted radius (namely it will be extracted within $\sim 4\%$ rather than with $\sim 3.7\%$). Lastly, the experiment plans to take sieve data with singles electrons at 575, 480 and 388 MeV/c as a check on the optics. In addition, elastic ep coincidence data will be taken at the same momentum settings as a check on the delta optics. This can also be studied with the pi0 production data.

In regard to the third point of the technical response, the small angle beam pipe has been used in the radiation budget.

7.2 Kinematical Settings

The kinematical settings are summarized in Table 1. The SHMS spectrometer will be set to access sequentially a range of Q^2 settings, and for each one of these settings the HMS spectrometer will in turn cover an extended phase space through a series of sequential sub-set of measurements. The kinematical phase space that will be covered by the measurements is shown in Fig. 10, after the first layer of acceptance cuts and phase space masking has been applied. A second layer of cuts will further bin the phase space in Q^2 and in θ_{pq}^* , as shown in Fig. 12. The beam current for the settings in groups *b*, *c*, and *d* will be $15 \mu\text{A}$. For the settings in group-*a* the beam current will be set to $6 \mu\text{A}$ so that the SHMS rate can stay below the 1 MHz level (note: recently, during the summer 2019 running period, we were able to operate the SHMS spectrometer at the 1.3 MHz rate without any concern, in a similar configuration during the E12-15-001 experiment). The HMS singles rate is at a comfortable level of a few tens of KHz for all the settings, as shown in Table 2. These rates have been calculated using the well established Wiser calculations for pions and protons, and the Bosted inelastic calculation folded with the SHMS acceptance for electron-singles. The signal-to-noise ratio (S/N), within a coincidence timing window of 1.5 ns , ranges between 1.2 and 7, as given in Table 1. Further suppression of accidentals can be achieved by applying a missing mass cut in the data analysis.

7.3 Data analysis and projected results

The cross section of the $p(e, e'p)\pi^\circ$ reaction is sensitive to a set of independent partial responses ($\sigma_T, \sigma_L, \sigma_{LT}, \sigma_{TT}$):

$$\frac{d^5\sigma}{d\omega d\Omega_e d\Omega_{pq}^{cm}} = \Gamma(\sigma_T + \varepsilon \cdot \sigma_L - v_{LT} \cdot \sigma_{LT} \cdot \cos \phi_{pq}^* + \varepsilon \cdot \sigma_{TT} \cdot \cos 2\phi_{pq}^*)$$

where $v_{LT} = \sqrt{2\varepsilon(1+\varepsilon)}$ is a kinematic factor, ε is the transverse polarization of the virtual photon, Γ is the virtual photon flux, and ϕ_{pq}^* is the proton azimuthal angle with respect to the electron scattering plane. The differential cross sections ($\sigma_T, \sigma_L, \sigma_{LT}, \sigma_{TT}$) are all functions of the center-of-mass energy W , the Q^2 , and the proton center of mass polar angle θ_{pq}^* (measured from the momentum transfer direction). The $\sigma_0 = \sigma_T + \varepsilon \cdot \sigma_L$ response is dominated by the M_{1+} resonant multipole while the interference of the $C2$ and $E2$ amplitudes with the $M1$ dominates the Longitudinal - Transverse and Transverse - Transverse responses, respectively. Cross section measurements will be performed at the nucleon resonance region, extending from $Q^2 = 0.015 (\text{GeV}/c)^2$ to $Q^2 = 0.055 (\text{GeV}/c)^2$ and covering the θ_{pq}^* range from 0° to 90° . For part of the θ_{pq}^* coverage, due to space limitations of the experimental setup, the proton spectrometer will be sequentially placed at $\phi_{pq}^* = 0^\circ$ and 180° , thus allowing to measure the in-plane azimuthal asymmetry of the cross section with respect to the momentum transfer direction, $A_{(\phi_{pq}=0,\pi)} = [\sigma_{\phi_{pq}=0} - \sigma_{\phi_{pq}=180}] / [\sigma_{\phi_{pq}=0} + \sigma_{\phi_{pq}=180}]$; this will in-turn enhance the sensitivity to the measurement of the Coulomb quadrupole amplitude. Here, for the pair of $\phi_{pq}^* = 0^\circ$ and 180° measurements, the cross sections and asymmetries will be obtained with the phase space matched in (W, Q^2, θ_{pq}^*) . A first level of

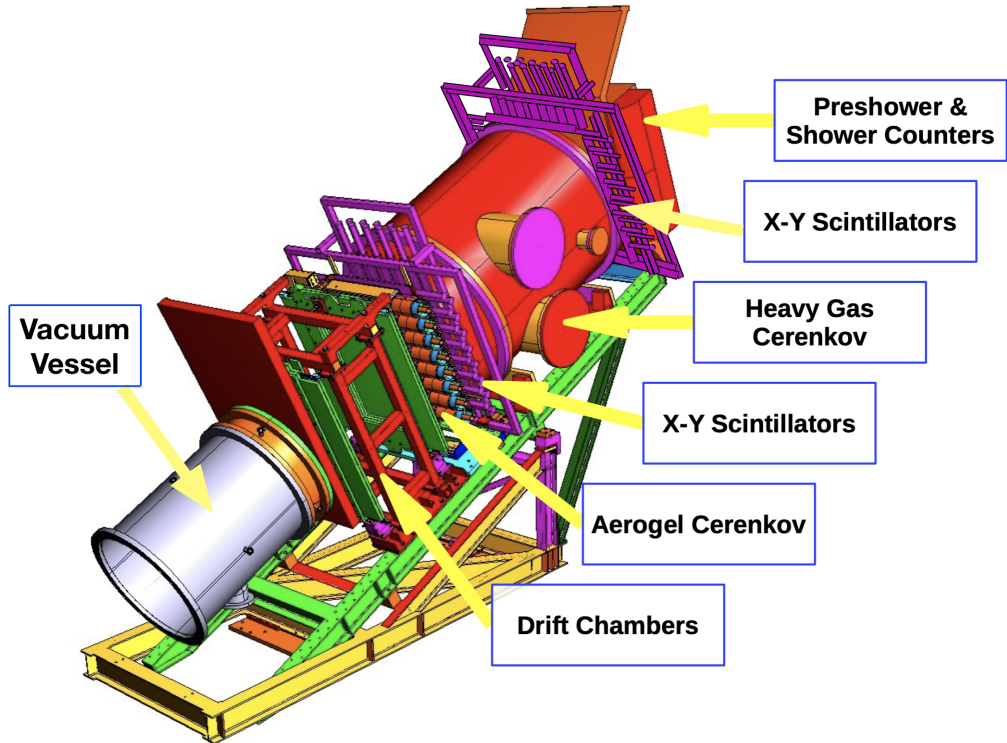


Figure 8. HMS Detector stack.

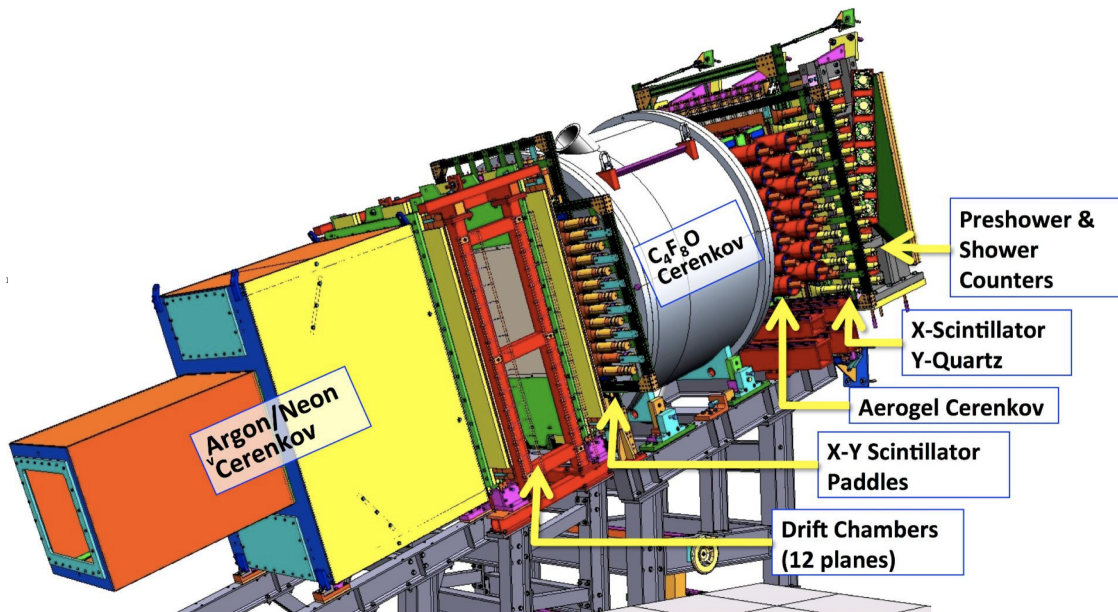


Figure 9. SHMS Detector stack. For this experiment, the standard SHMS configuration in which the Argon/Neon Cerenkov is replaced with a vacuum pipe will be used.

Setting	SHMS θ (deg)	SHMS P (MeV/c)	HMS θ (deg)	HMS P (MeV/c)	S/N	Time (hrs)
1a	7.29	952.26	18.77	532.53	2	7
2a			25.17	527.72	2	7
3a			33.7	506.61	3.2	6
4a			42.15	469.66	4.3	5
5a			50.44	418.56	4.9	5
6a			54.47	388.38	4.9	5
7a			12.37	527.72	2.7	6
1b	8.95	946.93	22.01	547.54	1.2	6
2b			28.24	542.61	1.4	6
3b			36.52	520.95	2.5	5
4b			44.64	483.08	3.4	4
5b			52.68	430.78	3.7	4
6b			56.53	399.92	3.5	4
7b			12.46	535.98	1.6	5
1c	10.37	941.61	24.40	562.00	1.5	9
2c			30.47	556.95	1.9	9
3c			38.52	534.79	3.5	6
4c			46.47	496.06	4.4	6
5c			54.17	442.64	4.8	6
6c			57.85	411.16	4.8	6
7c			12.69	543.24	2	6
1d	11.63	936.28	26.24	575.96	1.8	12
2d			32.16	570.80	2.5	11
3d			40.01	548.17	4.5	8
4d			47.73	508.64	5.5	8
5d			55.18	454.17	6.9	7
6d			58.71	422.13	6	8
7d			12.47	548.17	2.1	10

Table 1. The kinematical settings of the proposed measurements, utilizing an 1.3 GeV beam. The signal-to-noise ratio and the required beam time are given for each setting.

Setting	SHMS e ⁻ (KHz)	SHMS π^- (KHz)	HMS p (KHz)	HMS π^+ (KHz)
1a	970.2	5.04	5.1	25.6
2a			5.6	23.5
3a			5.3	19.1
4a			4.3	15.9
5a			3.2	14.8
6a			2.6	15.1
7a			4.0	23.8
1b	885.1	11.5	11.6	49.7
2b			11.8	42.7
3b			10.4	33.3
4b			8.2	27.7
5b			5.8	26.2
6b			4.7	27.3
7b			8.4	49.3
1c	510.0	12.0	11.9	45.3
2c			11.6	37.3
3c			9.8	28.4
4c			7.5	23.5
5c			5.2	22.9
6c			4.1	24.2
7c			8.6	49.1
1d	331.1	12.3	11.9	40.9
2d			11.2	32.8
3d			9.2	24.6
4d			6.9	20.5
5d			4.7	20.3
6d			3.6	21.7
7d			8.6	48.7

Table 2. Singles rates for the SHMS and the HMS spectrometers.

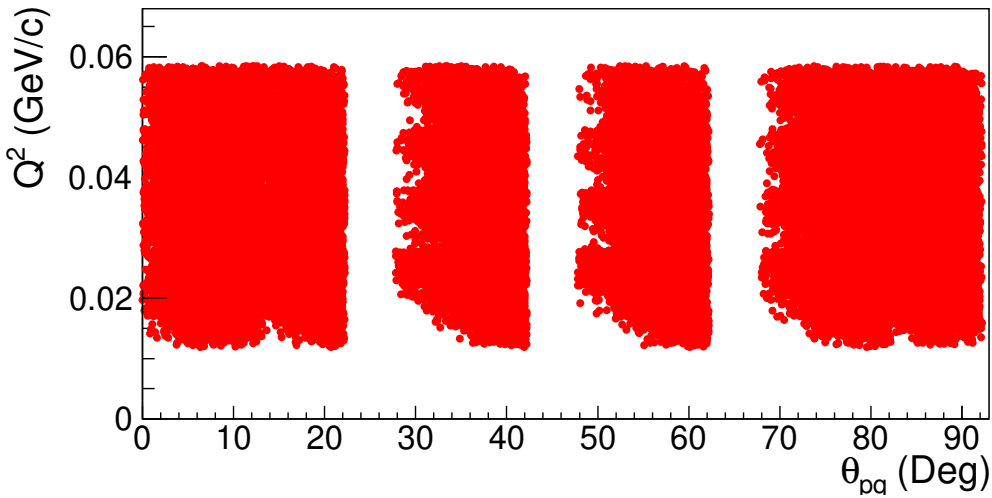


Figure 10. The phase space that will be accessed by the proposed measurements, after a first layer of acceptance cuts and phase space masking has been applied.

acceptance cuts will be applied in the data analysis aiming to limit the phase space to the central region of the spectrometers and to ensure that potential edge effects will be avoided, followed by a second layer of analysis cuts where the phase space will be further binned. Point cross sections will be extracted from the finite acceptances by utilizing the cross section calculations from the state of the art theoretical models^{52–54, 69, 70} in the Monte Carlo simulation, while radiative corrections will also be applied to the data analysis using the Monte Carlo simulation. The reconstructed missing mass spectrum is shown in Fig. 11. The effect of the systematic uncertainties has been based on Monte Carlo simulation studies and on the standard performance of the experimental setup. For the measured cross section, the overall systematic uncertainties will range from 2.8% to 3.8%, depending on the kinematics, dominating over the $\sim 1\%$ statistical uncertainties. The systematic uncertainties are driven by the level of understanding of the acceptance, the resolution of the experimental setup, the uncertainty of the beam energy and of the scattering angle, the beam charge determination, and to a smaller extent by the target density, detector efficiencies, target cell background, target length and dead time corrections. A break-down of the systematic uncertainties is given in Table 3. For the asymmetry measurements, the systematic uncertainties will be further suppressed through the cross section ratio. A second advantage is presented here, by the fact that the electron spectrometer position and momentum settings do not change during the asymmetry measurements. The projected level of systematic uncertainties is equivalent to the one demonstrated in similar measurements that we have performed in the past, with similar experimental setups and within a similar Q^2 range, at JLab and at MAMI^{26–29}. Furthermore, we recently had the opportunity to measure the same reaction channel, parasitically during the running of the E12-15-001 (VCS) experiment, with the exact same experimental setup (i.e. SHMS and HMS measuring electrons and protons in coincidence, respectively) at a slightly higher momentum transfer of $Q^2 = 0.3 \text{ (GeV/c)}^2$. The nearly final results of this data analysis confirms the well known cross section measurements in that region, well within the 3% level. The results have demonstrated an excellent understanding of the coincidence acceptance within the simulation and of the systematic uncertainties, as well as the readiness of all the experimental and theoretical tools involved in this effort. In Fig. 13 the comparison of the data with the simulation is presented for these measurements. The data have been corrected for all known efficiencies (and they are not arbitrarily normalized to the simulation). The simulation has been weighted with the MAID cross

Resolution	2% - 3%
Acceptance	1%
Scattering angle	0.4% - 0.6%
Beam energy	0.7% - 1.2%
Beam charge	1%
Target density	0.5%
Detector efficiencies	0.5%
Target cell background	0.5%
Target length	0.5%
Dead-time corrections	0.5%
Total	2.8% - 3.8%

Table 3. Summary table of the cross section systematic uncertainties.

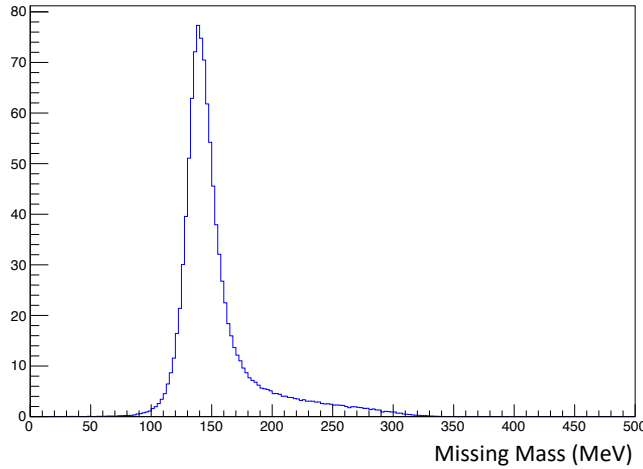


Figure 11. The missing mass spectrum, corresponding to the undetected pion.

section, which is known to describe the data very well in this kinematical region.

An aspect of these analysis that requires attention involves the treatment of the non-resonant pion electro-production amplitudes that interfere with the extraction of the resonant amplitudes in the $N \rightarrow \Delta$ transition. These interfering contributions, small in magnitude but large in number, can not be sufficiently constrained by the experimental measurements, and they thus result into a model uncertainty for the quadrupole transition form factors. In the past these contributions have been occasionally poorly studied or quoted as an uncertainty. Here, the effect of these amplitudes is studied by employing state of the art theoretical pion electroproduction models^{52–54, 69, 70} in the data analysis. Fits of the resonant amplitudes will be performed while taking into account the contributions of background amplitudes from the different models. The models offer different descriptions for the background amplitudes, leading to deviations in the extracted values of the transition form factors that are quantified as a model uncertainty. This uncertainty will in-turn be accounted for in the extraction of the G_E^n at each Q^2 . This procedure has been followed in the past in various experiments e.g. ^{26–29}. The good level of control over the model uncertainties has been validated in the past experimentally, through studies of the weak $p(e, e' p)\gamma$ excitation channel. In this case the same physics signal can be extracted within a different theoretical framework, thus offering an ideal cross-check to the model uncertainties associated with the pion electroproduction channel. The branching ratio of the photon channel is very small (0.6%), two orders of magnitude smaller compared

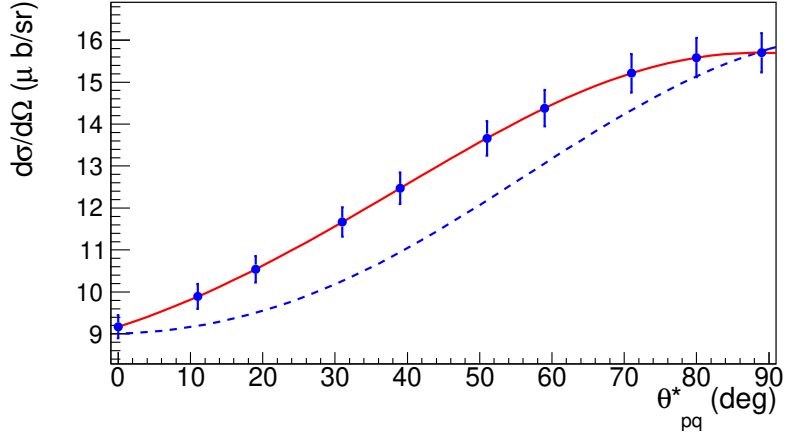


Figure 12. Projected cross section measurements at $Q^2 = 0.02 \text{ (GeV}/c)^2$ and $\phi_{pq}^* = 180^\circ$. The solid line shows the MAID cross section ($C2/M1=-4.5\%$). The dashed line shows the cross section prediction for $C2=0$.

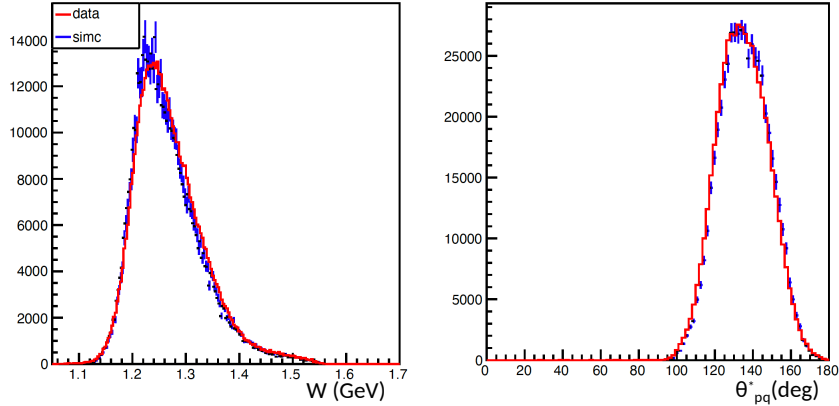


Figure 13. The parasitic measurement of the $p(e, e' p)\pi^0$ reaction at $Q^2 = 0.3 \text{ (GeV}/c)^2$ during the E12-15-001 (VCS) data taking. The simulation has been weighted with the MAID cross section. The same experimental arrangement will be used for the proposed measurements.

to the pion-electroproduction, and as such it was not studied until recently. To that end, the first such measurement was conducted at MAMI³⁰. Measurements for both channels were performed at the same Q^2 and utilizing the same experimental setup. The results were found in very good agreement between the two channels^{29,30}, thus giving credence to the quantification of the model uncertainties with the above procedure.

The projected measurements for the two quadrupole amplitudes are shown in Fig. 14. The G_E^n will be extracted following the procedure described in¹. The theoretical uncertainty in the G_E^n extraction is typically a factor of 2 smaller compared to the experimental uncertainty, as can be seen e.g. by the variance of the results in Fig. 5(a), and will thus not be a dominant factor in the neutron charge radius extraction. The projected G_E^n measurements are shown in Fig. 15. The G_E^n fit using the parametrization 6, as shown with the dashed line (the shaded band indicates the uncertainty of the fit), will allow to extract the slope at $Q^2 \rightarrow 0$ and the $\langle r_n^2 \rangle$ within $\sim 3.7\% (\pm 0.004 \text{ (fm})^2)$. The measurement will be of equivalent precision to the radius extraction that is based on the measurement of the neutron-electron scattering length. In

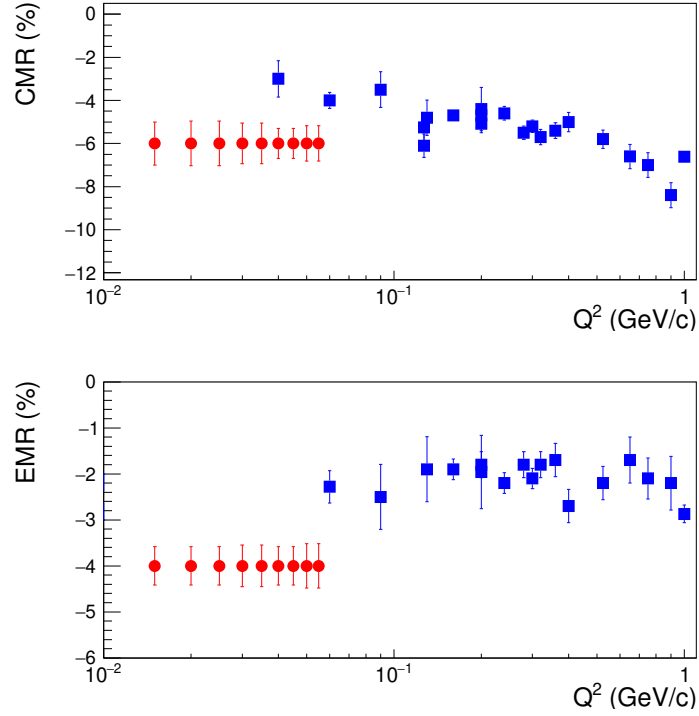


Figure 14. The projected CMR and EMR measurements (red) and the world data (blue).

Fig. 16 the fits within a limited fitting range at low Q^2 are shown, exhibiting the group of functions that can provide a good fit to the data. The low- Q^2 fits have the capacity to determine the $\langle r_n^2 \rangle$ with the same level of precision as the fits over the complete Q^2 range. The projected measurement for $\langle r_n^2 \rangle$ is shown in Fig. 17. Finally, the new G_E^n data will allow the flavor decomposition of the nucleon form factors, as described in the earlier sections; the projected measurements are shown in Fig. 6. From the $F_1^{u(d)}$ data, the mean square radius of the quark distributions $\langle b_{u(d)}^2 \rangle$ will be directly determined from $F_1^{u(d)}$ fits through Eq. 9.

8 Summary

The neutron is a cornerstone in our depiction of the visible universe. In this work we propose to measure the neutron charge radius, one of the system's most fundamental properties. A precise determination of the nucleon's size is unquestionably a critical step towards our understanding of the nucleon's structure. The neutron has proved to be a very challenging system to study in the lab. Contrary to the proton, the determination of the neutron charge radius has in the past relied solely on one method, the measurement of the *neutron-electron* scattering length. These results are characterized by longstanding discrepancies that have puzzled the physics community for two decades. They further illustrate the limitations of this method of charge radius extraction, pointing to underlying systematic uncertainties, and to our insufficient understanding of the neutron charge radius. Here, we propose to measure the neutron's charge radius using a new method¹ that takes advantage of the fundamental symmetry of the neutron and the proton, as opposed to relying on measurements with few-body nuclear targets that was done in the past. Following that path, we can overcome the limitations of previous methods and access otherwise inaccessible low momentum transfers, thus making a precise $\langle r_n^2 \rangle$ extraction possible. This will in-turn allow to improve the

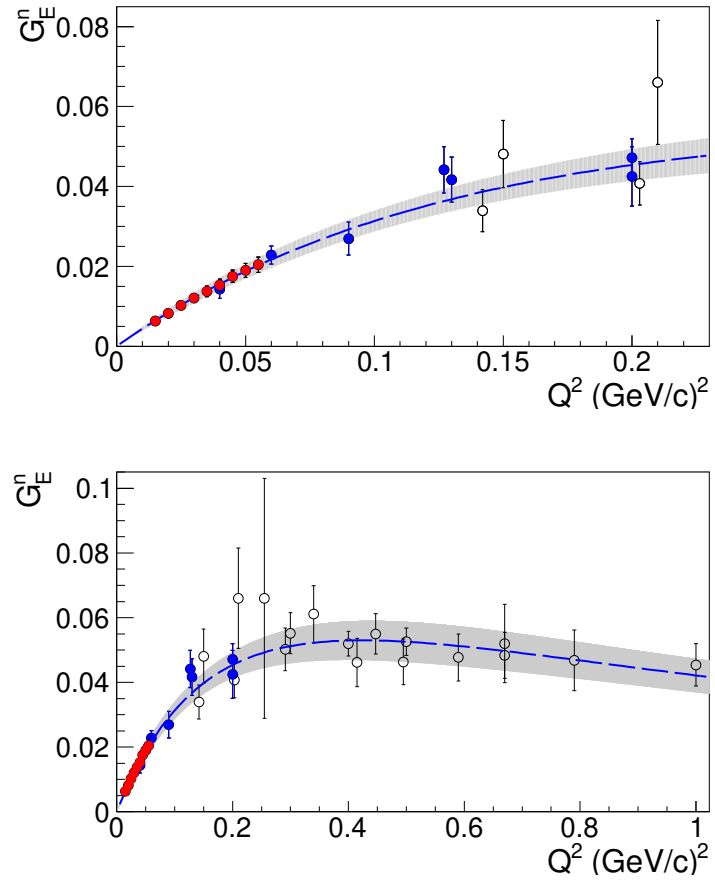


Figure 15. The (arbitrarily) projected G_E^n measurements (shown in red). The G_E^n world data from the polarization measurements (white) are shown, along with the G_E^n data from [1](#) (blue). The top panel shows a zoomed-in perspective of the low- Q^2 region.

precision, and the confidence, of the world data average value for $\langle r_n^2 \rangle$. The proposed measurements will also allow to resolve the long standing discrepancies in the measurement of the neutron-electron scattering length, that have implications in other areas of physics. Finally, considering our recent experience with the proton radius puzzle, one can note that for the first time an alternative method is presented here for a precise measurement of this fundamental quantity. The case of the proton has highlighted the value, the necessity and the scientific obligation to determine fundamental quantities with alternative methods, whenever possible.

The experiment will require standard Hall C equipment, namely a 4 cm liquid hydrogen target, an 1.3 GeV beam with $I = 15 \mu\text{A}$, and the SHMS and the HMS spectrometers with their standard detector packages, for the measurement of electrons and protons, respectively. The experiment will need to acquire data for 7.8 days at full efficiency, and an additional day for optics and normalization measurements, so that the $\langle r_n^2 \rangle$ can be determined within $\sim 3.7\%$.

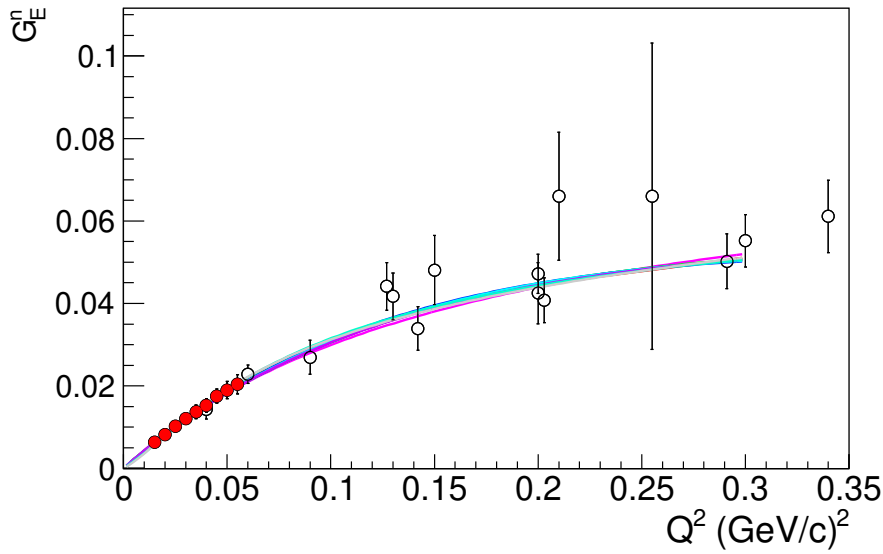


Figure 16. The low- Q^2 fits using a variety of functional forms, as in¹. The projected measurements from this proposal are shown in red.

References

1. Atac, H. *et al.* Measurement of the neutron charge radius and the role of its constituents. *Nature Communications* **12**, 1759 (2021).
2. Pohl, R. *et al.* The size of the proton. *Nature* **466**, 213–216 (2010).
3. R. Pohl, G. A. M., R. Gilman & Pachucki, K. Muonic hydrogen and the proton radius puzzle. *Ann. Rev. Nucl. Part. Sci.* **63**, 175–204 (2013).
4. Kopecky, S. *et al.* Neutron charge radius determined from the energy dependence of the neutron transmission of liquid Pb-208 and Bi-209. *Phys. Rev.* **C56**, 2229–2237 (1997).
5. Nico, J. & Snow, W. Fundamental neutron physics. *Ann. Rev. Nucl. Part. Sci.* **55**, 27–69 (2005).
6. Nesvizhevsky, V. *et al.* Neutron scattering and extra-short-range interactions. *Phys. Rev.* **D77**, 034020 (2008).
7. Koester, L. *et al.* Neutron electron scattering length and electric polarizability of the neutron derived from cross-sections of bismuth and of lead and its isotopes. *Phys. Rev.* **C51**, 3363–3371 (1995).
8. Aleksandrov, Yu. A., Vrana, M., Manrique, G. J., Machehkina, T. A. & Sedlakova, L. N. Neutron rms radius and electric polarizability from data on the interaction of slow neutrons with bismuth. *Sov. J. Nucl. Phys.* **44**, 900–902 (1986).
9. Krohn, V. E. & Ringo, G. R. Reconsiderations of the electron - neutron scattering length as measured by the scattering of thermal neutrons by noble gases. *Phys. Rev.* **D8**, 1305–1307 (1973).
10. Madey, R. *et al.* Measurements of G_E^n/G_M^n from the ${}^2H(\vec{e}, e' \vec{n}) {}^1H$ reaction to $Q^2 = 1.45$ (GeV/c) 2 . *Phys. Rev. Lett.* **91**, 122002 (2003).
11. Schlimme, B. S. *et al.* Measurement of the neutron electric to magnetic form factor ratio at $Q^2 = 1.58$ GeV^2 using the reaction ${}^3\vec{He}(\vec{e}, e' n) pp$. *Phys. Rev. Lett.* **111**, 132504 (2013).

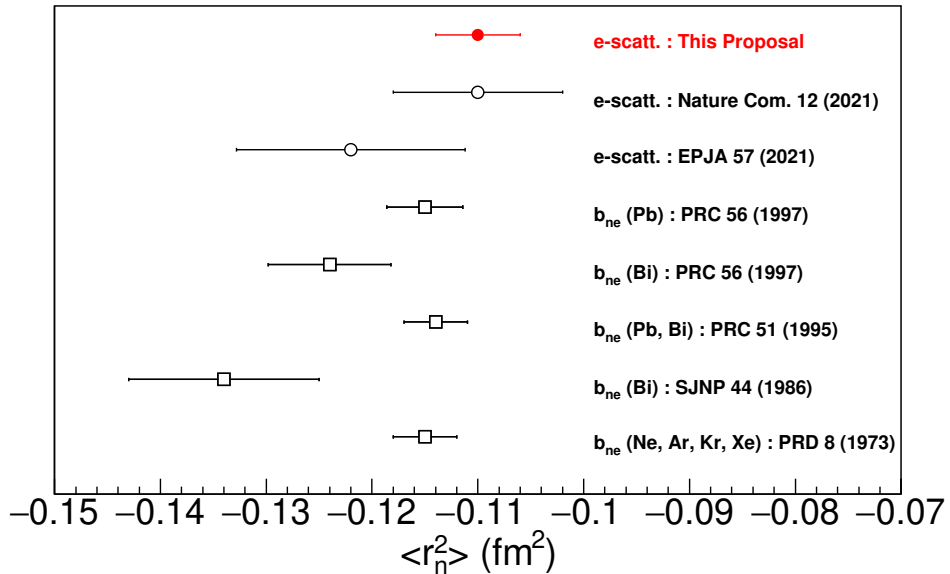


Figure 17. The proposed $\langle r_n^2 \rangle$ measurement is shown (red point) projected on the value extracted in¹. The b_{ne} measurements from the references^{4,7–9} that are included in the PDG analysis for the $\langle r_n^2 \rangle$ are shown (open-boxes). The electron scattering extraction measurements from^{1,75} are also shown (open-circles)

12. Riordan, S. *et al.* Measurements of the Electric Form Factor of the Neutron up to $Q^2=3.4\text{ GeV}^2$ using the Reaction ${}^3\vec{H}e(\vec{e},e'n)p$. *Phys. Rev. Lett.* **105**, 262302 (2010).
13. Glazier, D. I. *et al.* Measurement of the electric form-factor of the neutron at $Q^2 = 0.3\text{ (GeV}/c)^2$ to $0.8\text{ (GeV}/c)^2$. *Eur. Phys. J.* **A24**, 101–109 (2005).
14. Plaster, B. *et al.* Measurements of the neutron electric to magnetic form-factor ratio G_{En}/G_{Mn} via the ${}^2H(\vec{e},e',\vec{n}){}^1H$ reaction to $Q^2 = 1.45\text{ (GeV}/c)^2$. *Phys. Rev.* **C73**, 025205 (2006).
15. Zhu, H. *et al.* A Measurement of the electric form-factor of the neutron through $\vec{d}(\vec{e},e'n)p$ at $Q^2 = 0.5\text{ (GeV}/c)^2$. *Phys. Rev. Lett.* **87**, 081801 (2001).
16. Warren, G. *et al.* Measurement of the electric form-factor of the neutron at $Q^2 = 0.5$ and $1.0\text{ GeV}^2/c^2$. *Phys. Rev. Lett.* **92**, 042301 (2004).
17. Rohe, D. *et al.* Measurement of the neutron electric form-factor $G_{(en)}$ at $0.67\text{ (GeV}/c)^2$ via ${}^3\vec{H}e(\vec{e},e'n)$. *Phys. Rev. Lett.* **83**, 4257–4260 (1999).
18. Bermuth, J. *et al.* The Neutron charge form-factor and target analyzing powers from ${}^3\vec{H}e(\vec{e},e'n)$ scattering. *Phys. Lett.* **B564**, 199–204 (2003).
19. Geis, E. *et al.* The Charge Form Factor of the Neutron at Low Momentum Transfer from the ${}^2\vec{H}(\vec{e},e'n)p$ Reaction. *Phys. Rev. Lett.* **101**, 042501 (2008).
20. Eden, T. *et al.* Electric form factor of the neutron from the ${}^2\vec{H}(\vec{e},e'n){}^1H$ reaction at $Q^2=0.255\text{ (GeV}/c)^2$. *Phys. Rev. C* **50**, R1749–R1753 (1994).

21. Ostrick, M. *et al.* Measurement of the Neutron Electric Form Factor $G_{E,n}$ in the Quasifree $^2H(\vec{e}, e' \vec{n})p$ Reaction. *Phys. Rev. Lett.* **83**, 276–279 (1999).
22. Golak, J., Ziemer, G., Kamada, H., Witała, H. & Glöckle, W. Extraction of electromagnetic neutron form factors through inclusive and exclusive polarized electron scattering on a polarized 3He target. *Phys. Rev. C* **63**, 034006 (2001).
23. Herberg, C. *et al.* Determination of the neutron electric form-factor in the D(e,e' n)p reaction and the influence of nuclear binding. *Eur. Phys. J. A* **5**, 131–135 (1999).
24. Buchmann, A. J. Electromagnetic N $\rightarrow \Delta$ transition and neutron form-factors. *Phys. Rev. Lett.* **93**, 212301 (2004).
25. Pascalutsa, V. & Vanderhaeghen, M. Large- N_c relations for the electromagnetic nucleon-to- Δ form factors. *Phys. Rev. D* **76**, 111501(R) (2007).
26. Blomberg, A. *et al.* Electroexcitation of the $\Delta^+(1232)$ at low momentum transfer. *Phys. Lett. B* **760**, 267–272 (2016).
27. Stave, S. *et al.* Lowest Q^2 Measurement of the $\gamma^* p \rightarrow \Delta$ Reaction: Probing the Pionic Contribution. *Eur. Phys. J. A* **30**, 471–476 (2006).
28. Sparveris, N. *et al.* Measurements of the $\gamma^* p \rightarrow \Delta$ reaction at low Q^2 . *Eur. Phys. J. A* **49**, 136 (2013).
29. Sparveris, N. F. *et al.* Determination of quadrupole strengths in the $\gamma^* p \rightarrow \Delta(1232)$ transition at $Q^2 = 0.20 \text{ (GeV/c)}^2$. *Phys. Lett. B* **651**, 102–107 (2007).
30. Blomberg, A. *et al.* Virtual Compton Scattering measurements in the nucleon resonance region. *Eur. Phys. J. A* **55**, 182 (2019). [1901.08951](#).
31. A. de Rujula, H. G. & Glashow, S. *Phys. Rev. D* **12**, 147 (1975).
32. Glashow, S. *Physica* **96A**, 27 (1979).
33. Bernstein, A. & Papanicolas, C. Shapes of hadrons. *AIP Conf. Proc.* **904**, 1 (2007).
34. Bernstein, A. *Eur. Phys. J. A* **17**, 349 (2003).
35. N. Isgur, G. K. & Koniuk, R. *Phys. Rev. D* **25**, 2394 (1982).
36. Capstick, S. & Karl, G. *Phys. Rev. D* **41**, 2767 (1990).
37. Blanpied, G. *Phys. Rev. Lett.* **79**, 4337 (1997).
38. Beck, R. *et al.* *Phys. Rev. Lett.* **78**, 606 (1997).
39. Beck, R. *et al.* *Phys. Rev. C* **61**, 035204 (2000).
40. Frolov, V. *et al.* *Phys. Rev. Lett.* **82**, 45 (1999).
41. Pospischil, T. *et al.* *Phys. Rev. Lett.* **86**, 2959 (2001).
42. Mertz, C. *et al.* *Phys. Rev. Lett.* **86**, 2963 (2001).
43. Bartsch, P. *et al.* *Phys. Rev. Lett.* **88**, 142001 (2002).
44. van Buuren, L. *et al.* *Phys. Rev. Lett.* **89**, 012001 (2002).
45. van Buuren, L. *et al.* *Phys. Rev. C* **70**, 042201 (2004).
46. Kunz, C. *et al.* *Phys. Lett. B* **564**, 21 (2003).

47. Sparveris, N. F. *et al.* Investigation of the conjectured nucleon deformation at low momentum transfer. *Phys. Rev. Lett.* **94**, 022003 (2005).
48. Kelly, J. *Phys. Rev. Lett.* **95**, 102001 (2005).
49. Kelly, J. J. *et al.* Recoil polarization measurements for neutral pion electroproduction at $Q^2 = 1$ (GeV/c) 2 near the Delta resonance. *Phys. Rev. C* **75**, 025201 (2007).
50. Ungaro, M. *et al.* *Phys. Rev. Lett.* **97**, 112003 (2006).
51. Alexandrou, C. *et al.* *Phys. Rev. Lett.* **94**, 021601 (2005).
52. Sato, T. & Lee, T. Dynamical study of the Delta excitation in N (e, e-prime pi) reactions. *Phys. Rev. C* **63**, 055201 (2001).
53. Kamalov, S. & Yang, S. N. Pion cloud and the Q^2 dependence of $\gamma^* N \longleftrightarrow \Delta$ transition form-factors. *Phys. Rev. Lett.* **83**, 4494–4497 (1999).
54. Kamalov, S., Chen, G.-Y., Yang, S.-N., Drechsel, D. & Tiator, L. Pi0 photoproduction and electroproduction at threshold within a dynamical model. *Phys. Lett. B* **522**, 27–36 (2001).
55. SAID. <http://gwdac.phys.gwu.edu>.
56. Elsner, D. *et al.* Measurement of the LT-asymmetry in π^0 electroproduction at the energy of the $\Delta(1232)$ resonance. *Eur. Phys. J. A* **27**, 91–97 (2006).
57. Stave, S. *et al.* *Phys. Rev. C* **78**, 024209 (2008).
58. Aznauryan, I. G. *et al.* Electroexcitation of nucleon resonances from CLAS data on single pion electroproduction. *Phys. Rev. C* **80**, 055203 (2009).
59. Villano, A. N. *et al.* *Phys. Rev. C* **80**, 035203 (2009).
60. van Buuren, L. *et al.* *Phys. Rev. C* **84**, 028201 (2011).
61. D.-H. Lu, A. W. T. & Williams, A. G. *Phys. Rev. C* **55**, 3108 (1997).
62. U. Meyer, E. H. & Buchmann, A. J. *Phys. Rev. C* **64**, 035203 (2001).
63. M. Fiolhais, B. G. & Sirca, S. *Phys. Lett. B* **373**, 229 (1996).
64. Pascalutsa, V. & Vanderhaeghen, M. *Phys. Rev. D* **73**, 034003 (2006).
65. Gail, T. A. & Hemmert, T. R. *Eur. Phys. J A* **28**, 91 (2006).
66. Sanctis, M. D. *et al.* *Nucl. Phys. A* **755**, 294 (2005).
67. Mandeville, J. *et al.* *Phys. Rev. Lett.* **72**, 3325 (1994).
68. Alexandrou, C. *et al.* Proton and neutron electromagnetic form factors from lattice QCD. *Phys. Rev. D* **100**, 014509 (2019).
69. Drechsel, D., Hanstein, O., Kamalov, S. S. & Tiator, L. A Unitary isobar model for pion photoproduction and electroproduction on the proton up to 1-GeV. *Nucl. Phys. A* **645**, 145–174 (1999).
70. Arndt, R. A., Briscoe, W. J., Strakovsky, I. I. & Workman, R. L. Analysis of pion photoproduction data. *Phys. Rev. C* **66**, 055213 (2002).
71. Ye, Z., Arrington, J., Hill, R. J. & Lee, G. Proton and Neutron Electromagnetic Form Factors and Uncertainties. *Phys. Lett. B* **777**, 8–15 (2018).
72. Xiong, W. *et al.* A small proton charge radius from an electron–proton scattering experiment. *Nature* **575**, 147–150 (2019).

73. Galster, S. *et al.* Elastic electron-deuteron scattering and the electric neutron form factor at four-momentum transfers $5\text{fm}^{-2} < q^2 < 14\text{fm}^{-2}$. *Nucl. Phys. B* **32**, 221–237 (1971).
74. Cates, G. D., de Jager, C. W., Riordan, S. & Wojtsekhowski, B. Flavor decomposition of the elastic nucleon electromagnetic form factors. *Phys. Rev. Lett.* **106**, 252003 (2011).
75. Atac, H. *et al.* Charge radii of the nucleon from its flavor dependent Dirac form factors. *Eur. Phys. J. A* **37**, 65 (2021).